Title	Small-signal model of the two-phase interleaved coupled-inductor boost converter
Authors	Barry, Brendan C.;Hayes, John G.;Rylko, Marek S.;Stala, Robert;Penczek, Adam;Mondzik, Andrzej;Ryan, Robert T.
Publication date	2017-10-23
Original Citation	Barry, B. C., Hayes, J. G., Rylko, M. S., Stala, R., Penczek, A., Mondzik, A. and Ryan, R. T. (2017) 'Small-signal model of the two-phase interleaved coupled-inductor boost converter', IEEE Transactions on Power Electronics, 33(9), pp. 8052-8064. doi: 10.1109/TPEL.2017.2765920
Type of publication	Article (peer-reviewed)
Link to publisher's version	10.1109/TPEL.2017.2765920
Rights	© 2017, IEEE. Personal use of this material is permitted. Permission from IEEE must be obtained for all other uses, in any current or future media, including reprinting/republishing this material for advertising or promotional purposes, creating new collective works, for resale or redistribution to servers or lists, or reuse of any copyrighted component of this work in other works.
Download date	2025-09-03 13:05:23
Item downloaded from	https://hdl.handle.net/10468/11786

Please note that this is the accepted version, the IEEE published version can be found by linking to IEEE *Xplore* [®] or the DOI.

Small-Signal Model of the Two-Phase Interleaved Coupled-Inductor Boost Converter

Brendan C. Barry[1], *Member, IEEE*, John G. Hayes[1], *Member, IEEE,* Marek S. Ryłko[2], *Member, IEEE*, Robert Stala[2], Adam Penczek[2], Andrzej Mondzik[2], and Robert T. Ryan[1], *Student Member, IEEE*.

[1]Power Electronics Research Laboratory, School of Engineering, University College Cork, Ireland
[2]SMA Magnetics Sp. z o.o., 32-080, Zabierzow, ul. Krakowska 390, Poland

Corresponding author:	Dr. Brendan Barry
Address:	University College Cork, College Rd. Cork, Ireland
Tel.:	+353 86 8616737
Email:	110110038@umail.ucc.ie

Abstract – **A coupled-inductor dc-dc converter has several modes of operation in CCM and DCM, and is quite complex. This paper presents the derivation of the complete small-signal model of a two-phase interleaved dc-dc boost converter utilizing a single-core coupled-inductor operating in both CCM and DCM. Several small-signal models are required to fully model the converter due to the complexity of the converter operating in DCM. The transfer functions are then derived from these small-signal models. The theoretical analysis is validated experimentally using frequency sweeps from a 1 kW prototype.**

Keywords – Coupled-inductors, Interleaved boost, Small-signal, DC-DC Converters

NOMENCLATURE

v_i	Converter input voltage	R_o	Converter load equivalent output resistance
v_o	Converter output voltage	R_C	Output capacitor equivalent series resistance
v_L	Phase inductor voltage	R_L	Coupled-inductor equivalent series resistance
v_{Lk}	Leakage inductance back emf	d_c	Converter duty cycle
v_T	Magnetizing inductance back emf	d_{off}	Diode current conduction time
i_{Co}	Output capacitor current	d_x	Cycle time of sub-mode x
i_o	Load current	T	Converter switching cycle period
$i_{o,Bmax}$	Maximum load current at boundary	f_s	Converter switching frequency
i_{L1}	Inductor current in phase 1	C_{eq}	Equivalent output capacitance
i_{L2}	Inductor current in phase 2	CCM	Continuous-Conduction Mode
i_{S1}	Switch current in phase 1	DCM	Discontinuous-Conduction Mode
i_{S2}	Switch current in phase 2	ESR	Equivalent-Series-Resistance
i_{D1}	Diode current in phase 1	1L	Single-phase
i_{D2}	Diode current in phase 2	2L	Two-phase
i_m	Magnetizing current	CL	Coupled-inductor
Δi_{mx}	Magnetizing current change during sub-mode x	XL	Interphase transformer
L	Phase inductance	α	Unified transfer function coefficient
L_{Lk}	Leakage inductance	β	Unified transfer function coefficient
L_m	Magnetizing inductance	γ	Unified transfer function coefficient
C_o	Output capacitance	δ	Unified transfer function coefficient

I. INTRODUCTION

A wide range of applications, including commercial, industrial, transportation, renewable energies and aeronautics, utilize high-power, high-efficiency dc-dc converters. For example, a fuel cell vehicle is reliant on a high-power boost converter to efficiently distribute a stable voltage to the traction inverters [1]-[3]. One of the main design considerations of dc-dc converters, especially in transport and aeronautics, is the size and weight of the magnetic components [4]. Single-phase (1L) boost converters are common

in industry due to the relative ease of implementation. However, high-power, high-current applications often incorporate multi-phase converters, such as a two-phase (2L) converter, in order to reduce the necessary current rating on the semiconductor switches [5]. Another advantage of multi-phase converters is the size reduction of the magnetic components due to the decreased current flowing through the windings. This size reduction can be extended further by incorporating two or more of the phases onto a single inductor core. These types of single-core, multi-phase inductors are referred to as coupled-inductors (CL) or integrated-magnetics (IM) [6]-[9]. A converter featuring the 1L, 2L, and CL options is presented in Fig. 1 [10]. Suitably designed coupled-inductors can bring significant size reduction in the converter magnetic components when compared to traditional discrete inductors [11]. The coupled inductor used in the experimental testing in this paper, the CCTT IM, presented in Fig. 2, shows not only a reduction in weight, but also greater efficiency, particularly at partial load [12].

Implementing coupled-inductors in multi-phase dc-dc converters produces cross-coupling between the phases. This cross-coupling causes a decrease in inductor current ripple when operating in continuous-conduction mode (CCM). This allows a higher dc current to pass through the system, while ensuring the peak of the inductor current ripple does not saturate the core. When in CCM, the relationship between input voltage, output voltage and duty cycle is identical to that of a 2L system, but operation of a CL converter becomes much more complex in DCM. Several modes of operation are found to exist, each with their own converter gain and current waveforms. These modes are mapped in what is termed the CL boost converter CCM-DCM mode map, presented in Fig. 3. This mode map is used to easily determine which duty cycle yields the required output voltage for a given input voltage and output current, as well as the mode of operation of the converter. The mode map plots the converter duty cycle against the load current; normalized to $I_{o,Bmax}$, the maximum output current between the boundary between CCM and DCM. The derivation of each of these modes, as well as the mode map, is well documented in [10].

As can been seen from the mode map in Fig.3, there are up to ten different modes of operation in the CL boost converter; eight in DCM and two in CCM. While the large- and small-signal characteristics of CCM 1 and CCM 2 are identical, the same cannot be said for the different DCM modes. It is evident from Fig. 3 that when the converter is operating in DCM 5, a change in duty cycle does not cause a change in current, allowing this mode to be eliminated from analysis. Hence, for each converter configuration, eight modes of operation remain.
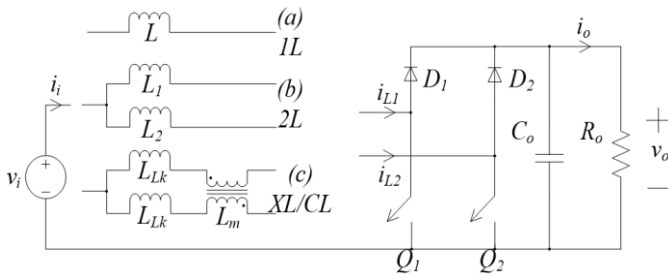

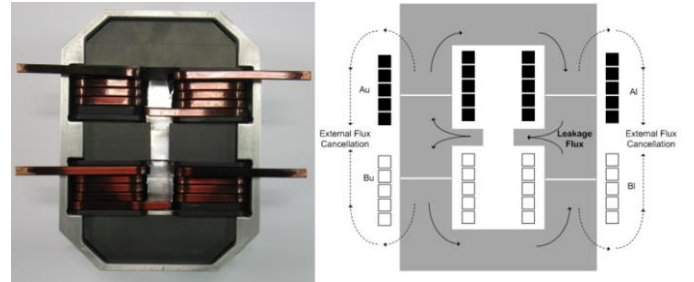Fig. 1. 1L, 2L and CL boost converter topologies.
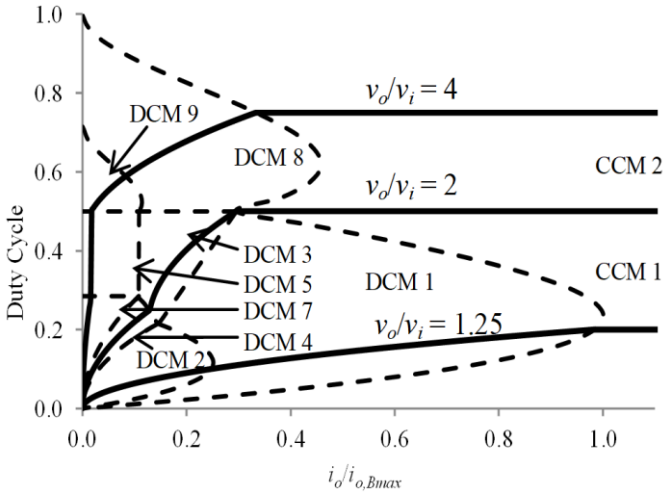

Fig. 2. CCTT IM coupled inductor.

Fig. 3. The CCM/DCM mode maps of the CL boost converter [13].

The final item to note on Fig. 3 is that the mode maps are dependent on the type of semiconductor switch used for Q_1 and Q_2 in Fig. 1. For the work carried out in this paper, a MOSFET with a free-wheeling diode is utilized, allowing for the flow of current to reverse. This is important due to the fact that current briefly flows from ground back through the switch and inductor when operating in DCM 5 and DCM 7. If a reverse blocking IGBT (RB IGBT) were implemented, the mode map presented in Fig. 3 would be slightly different, and a separate mode map would need to be developed [10].

Accurate transfer functions are essential in developing high-performance controllers for switch-mode power supplies. Several papers yield the small-signal models of individual dc-dc converters, such as the buck [13]-[14], boost [15]-[16], buck-boost [17] and flyback converters [18]. Many papers present both the large-signal, and small-signal models of multi-phase converters using discrete and coupled-inductors. For example, a two-phase interleaved buck converter is analyzed for operation in High-Intensity Discharge (HID) lamps using an averaged state-space representation in [19]. However, the inductors are discrete, and DCM operation is not included. A 16-phase bidirectional converter for hybrid vehicle applications, presented in [20], operates in DCM in order to improve current-balancing performance in each phase. In this reference, while a single-loop, digital Proportional-Integral (PI) controller is implemented using an FPGA, the model used to design the controller is not discussed. An interleaved power-factor-correction (PFC) boost converter is digitally controlled using sliding-mode control in [21]. Once again, this paper presents an averaged state-space representation. However, the converter is operated in CCM, with discrete inductors. An analysis presented in [22] provides a DCM state-space model of an interleaved boost converter which includes converter parasitic, but is once again only concerned with the discrete inductor topology.

As can be seen in Fig. 1, the CL converter analyzed in this paper is an inversely-coupled inductor. A comparison of 2L, CL directly-coupled, and CL inversely-coupled boost converter small-signal models is presented in [23]. The authors of this paper verify that inversely-coupled inductors have a high bandwidth in the closed-loop system, and a high quality factor. However, once again this analysis focuses on CCM operation.

A great deal of research has been done in the area of accurately developing unified small-signal models of dc-dc converters operating in both CCM and DCM [24]-[28]. Among these techniques is the development of a Signal-Flow Graph (SFG) [29]-[30]. An SFG is a graphical tool in which system variables, represented as nodes, are connected to each other via functions, which represented by branches. SFGs can be used to present both the large-signal and small-signal models of a system. However, a system must still be linearised before the small-signal model is developed.

As can be seen from this discussion, while there are many models of both discrete inductor and coupled-inductor CCM multi-phase boost converters, as well as many methods to derive these models, little to no research has been presented on the small-signal modeling of DCM operation when utilizing coupled-inductors. This paper focuses on the development of accurate small–signal models of each DCM mode of operation of a two-phase interleaved coupled-inductor boost converter. Section II derives the dynamic equations of the leakage inductance voltage drop and output capacitor current of the CL boost converter. Section III then uses the results of Section II to find the small-signal models and transfer functions of the CL boost converter operating in CCM. This allows for a relatively simple introduction to a CL boost converter for those who are only familiar with discrete inductor

converters, due to the fact that when a CL boost converter is operated in CCM, the results of the small-signal model are near identical to that of a 2L boost converter. Section IV outlines the equivalent analysis for DCM operation. Regarding DCM analysis, DCM 1 and DCM 4 are used as examples for the CL converter. The analysis can then be extended to all other DCM modes of operation. Section IV presents experimental frequency sweeps from a 1 kW CL boost converter laboratory prototype which are used to verify each DCM mode small-signal model. An earlier version of the work presented in this paper is discussed in [31], while a method of controlling each of the DCM modes of operation is presented in [32]. Finally, the appendix includes all formulae needed to reproduce the analysis presented in Section III to derive the small-signal models of all DCM modes of operation.

II. DYNAMIC EQUATIONS OF THE TWO-PHASE INTERLEAVED CL BOOST CONVERTER

This section details the derivation of the dynamic equations of the CL boost converter which can be used to determine the small-signal models of all operating modes of the converter, be they CCM or DCM. The small-signal models presented are based on the average model of the converter [33]. In order to simplify the analysis, it is assumed that both phases of the converter are balanced i.e.

$$
\begin{aligned}
i_{L1} &= i_{L2} \\
L_{Lk1} &= L_{Lk1} = L_{Lk} \\
d_{c1} &= d_{c2} = d_c \\
d_{off1} &= d_{off2} = d_{off}
\end{aligned}
\tag{1}
$$

where L_{Lkx}, i_{Lx}, d_{cx}, and d_{offx} are the leakage inductance, phase current, duty cycle (or switch conduction time), and diode conduction time of phase x, (1 or 2). The CL boost converter is presented in Fig. 4.
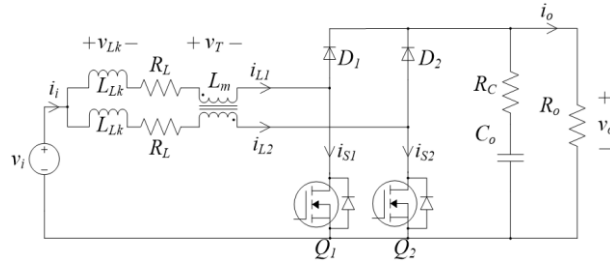

Fig. 4. The two-phase interleaved boost converter.

In all modes of the CL converter, there are two distinct sub-modes: the switch conduction time and the diode conduction time. The switch conduction time is determined by the duty cycle, d_c. During this part of the cycle the switch is closed, and current flows though the inductor and into the switch. Energy in the inductor builds up, and the current through the inductor rises to its peak value. When the switch opens, current flows through the diode and into the output filter and load for a period of the cycle labeled d_{off}. During this part of the cycle, the energy stored in the inductor is released into the load, and the current flowing through the inductor drops to its minimum value. When operating in CCM, the minimum value of the current is always greater than zero. However, when operating in DCM, the minimum value of the current always reaches zero, and in some cases, becomes negative.

In a CL boost converter, when the switch is closed, the input and output of the converter are disconnected from each other. The leakage inductance voltage v_{Lk} in this state is expressed as

$$
v_{Lk} = L_{Lk} \frac{di_{L1}}{dt} = v_i - v_T - i_{L1}R_L
\tag{2}
$$

where v_i is the converter input voltage, v_T is the voltage drop across the magnetizing inductance, i_{L1} is the inductor current of phase 1, and R_L is the coupled-inductor per-phase equivalent-series-resistance (ESR). When the switch is open and the diode conducts, the input and output are directly connected to each other, and the inductor voltage v_{Lk} in this state is expressed as

$$v_{Lk} = L_{Lk} \frac{di_{L1}}{dt} = v_i - v_o - v_T - i_{L1}R_L \tag{3}$$

where v_o is the converter output voltage. By averaging (2) with (3), the dynamic equation of the inductor voltage of the CL boost converter are found as

$$L_{Lk} \frac{di_{L1}}{dt} = d_c v_i + d_{off}(v_i - v_o) - v_T - i_{L1}R_L = v_i(d_c + d_{off}) - d_{off}v_o - (d_c + d_{off})v_T - (d_c + d_{off})i_{L1}R_L \tag{4}$$

Similarly, the output capacitor current i_{Co} of the converter during the full cycle is

$$i_{Co} = C_o \frac{dv_c}{dt} = i_{L1} + i_{L2} - i_{S1} - i_{S2} - \frac{v_o}{R_o} \tag{5}$$

where C_o is the output capacitance, R_o is the output load resistance, i_{Sx} is the dc switch current flowing through phase x, and v_c is the voltage drop across the capacitance. By applying Kirchoff's current law to the output filter of the converter, and finding the capacitor voltage in terms that are known, the capacitor voltage can be expressed as

$$v_c = \left(1 + \frac{R_C}{R_o}\right)v_o - 2R_C(i_{L1} - i_{S1}) \tag{6}$$

where R_C is the output capacitor ESR. By inserting (6) into (5) and applying the assumptions given in (1), the dynamic equation of the output capacitor of the CL boost converter is

$$C_{eq} \frac{dv_o}{dt} = 2i_{L1} - 2i_{S1} + 2C_o R_C \left(\frac{di_{L1}}{dt} - \frac{di_{S1}}{dt}\right) - \frac{v_o}{R_o} \tag{7}$$

where

$$C_{eq} = C_o \left(1 + \frac{R_C}{R_o}\right) \tag{8}$$

The equations presented in (4) and (7) can be used to describe the CL boost converter when operating in CCM and in any DCM mode. Hence, equations (4) and (7) are used as the starting point for all further analysis. It should be noted that whilst there is a third sub-mode of operation when the converter is in DCM, no current flows in either phase during this time from the point of view of phase 1, and so, it can be eliminated from the analysis. This sub-more is shown as D_6 in Fig. 6. If the analysis of phase 2 were to be undertaken, then it would be shown as D_3 in Fig. 6.

III. Continuous-conduction Mode Small-signal Model

The quantities v_T and i_{S1} must be found in order to utilize the equations presented in (4) and (7). These are derived by analyzing the inductor current waveforms of the operating mode of the converter. This section analyzes CCM operation of the CL converter, the waveforms of which are presented in Fig. 5 for a duty cycle less than 0.5.
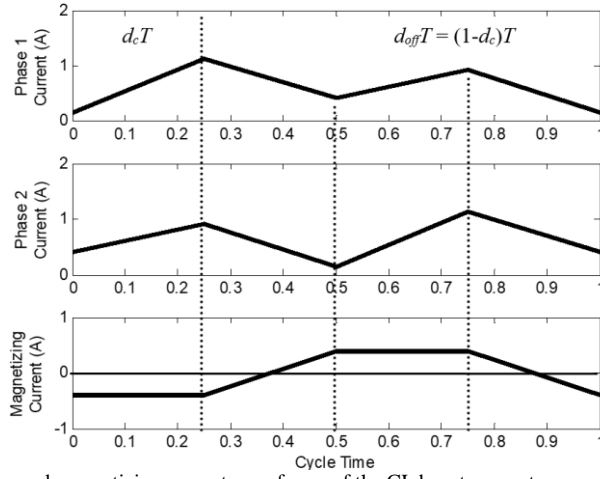
Fig. 5. Phase and magnetizing current waveforms of the CL boost converter operating in CCM.

The magnetizing inductance voltage drop v_T is dependent on the magnetizing current circulating through the inductor:

$$v_T = L_m \frac{di_m}{dt} \tag{9}$$

However, as can be seen from Fig. 5, the average change of the magnetizing current over one full cycle is zero:

$$(d_c + d_{off})v_T = 0 \tag{10}$$

The switch current i_{S1} is found as the dc inductor current of the converter averaged over the duty cycle:

$$i_{S1} = d_c i_{L1} \tag{11}$$

By inserting equation (10) into (4) and (11) into (7), the dynamic equations of the CCM CL boost converter are found as

$$L_{Lk} \frac{di_{L1}}{dt} = v_i - v_o - d_c v_o - i_{L1} R_L \tag{12}$$

$$C_{eq} \frac{dv_o}{dt} = 2i_{L1}(1 - d_c) + 2C_o R_C \frac{di_{L1}}{dt}\left(1 - \frac{dd_c}{dt}\right) - \frac{v_o}{R_o} \tag{13}$$

The equations presented in (12) and (13) must now be linearized before the small-signal model is found. In order to linearize the states of the converter, the following linearization method is applied [34].

When linearizing, if

$$\frac{dx}{dt} = f(x, y)$$

then

$$\frac{dx}{dt} = \frac{\partial f(x, y)}{\partial X} x + \frac{\partial f(x, y)}{\partial Y} y$$

Where a lowercase letter is used to represent a variable, which includes a steady-state dc operating point (X and Y) plus a small ac perturbation ($\tilde{x}$ and $\tilde{y}$). Hence, the states of the converter, once linearised, transform into

$$v_i = V_I + \tilde{v}_i(t)$$
$$v_o = V_O + \tilde{v}_o(t)$$
$$i_{L1} = I_{L1} + \tilde{i}_{L1}(t)$$
$$d_c = D_C + d_c(t)$$

For example, linearizing the inductor voltage equation presented in (12) yields

$$\frac{\partial\left[L_{Lk}\dfrac{di_{L1}(t)}{dt}\right]}{\partial\left[\dfrac{di_{L1}(t)}{dt}\right]}\frac{d\tilde{i}_{L1}(t)}{dt} = L_{Lk}\frac{d\tilde{i}_{L1}(t)}{dt} \tag{14}$$

$$\frac{\partial}{\partial v_i}\left[L_{Lk}\frac{di_{L1}(t)}{dt}\right]\tilde{v}_i(t) = \tilde{v}_i(t) \tag{15}$$

$$\frac{\partial}{\partial v_o}\left[L_{Lk}\frac{di_{L1}(t)}{dt}\right]\tilde{v}_o(t) = -(1-D_C)\tilde{v}_o(t) \tag{16}$$

$$\frac{\partial}{\partial d_c}\left[L_{Lk}\frac{di_{L1}(t)}{dt}\right]d_c(t) = V_O d_c(t) \tag{17}$$

$$\frac{\partial}{\partial i_{L1}}\left[L_{Lk}\frac{di_{L1}(t)}{dt}\right]\tilde{i}_{L1}(t) = R_L \tag{18}$$

Hence, the small-signal model of the inductor voltage is found to be

$$L_{Lk}\frac{d\tilde{i}_{L1}(t)}{dt} = \tilde{v}_i(t) - (1-D_C)\tilde{v}_o(t) + V_O d_c(t) - R_L\tilde{i}_{L1} \tag{19}$$

By linearising (13) in the same manner the small-signal model of the output capacitor current is found as

$$C_{eq}\frac{d\tilde{v}_o(t)}{dt} = 2(1-D_C)\tilde{i}_{L1}(t) - 2I_{L1}d_c(t) + 2C_oR_C(1-D_C)\frac{d\tilde{i}_{L1}(t)}{dt} - 2C_oR_CI_{L1}\frac{dd_c(t)}{dt} - \frac{\tilde{v}_o(t)}{R_o} \tag{20}$$

With the equations linearised, they are next transformed into the Laplace domain, i.e.

$$sL_{Lk}\tilde{i}_{L1}(s) = \tilde{v}_i(s) - (1-D_C)\tilde{v}_o(s) + V_O d_c(s) - R_L\tilde{i}_{L1}(s) \tag{21}$$

$$sC_{eq}\tilde{v}_o(s) = 2(1-D_C)\tilde{i}_{L1}(s) - 2I_{L1}d_c(s) + 2sC_oR_C(1-D_C)\tilde{i}_{L1}(s) - 2sC_oR_CI_{L1}d_c(s) - \frac{\tilde{v}_o(s)}{R_o} \tag{22}$$

In order to simplify the expressions, (21) and (22) can be rewritten into what are termed the unified small-signal models, i.e.

$$sL_{Lk}\tilde{i}_{L1}(t) = \alpha_1\tilde{v}_i(s) + \beta_1\tilde{v}_{out}(s) + \gamma_1 d_c(s) + \delta_1\tilde{i}_{L1}(s) \tag{23}$$

$$sC_{eq}\tilde{v}_o(s) = \alpha_2\tilde{v}_i(s) + \beta_2\tilde{v}_o(s) + \gamma_2 d(s) + \delta_2\tilde{i}_{L1}(s) \tag{24}$$

where the α, β, γ, and δ coefficients are what are termed the unified model coefficients, which for CCM are

$$\begin{aligned}
\alpha_1 &= 1 \\
\beta_1 &= -(1-D_C) \\
\gamma_1 &= V_O \\
\delta_1 &= -R_L \\
\alpha_2 &= 0 \\
\beta_2 &= -\frac{1}{R_o} \\
\gamma_2 &= -2I_{L1}(1+C_oR_Cs) \\
\delta_2 &= 2(1+C_oR_Cs)(1-D_C)
\end{aligned} \tag{25}$$

Equations (23) and (24) are now coupled with the coefficients provided in (25), and the small-signal model of the CL converter operating in CCM is now complete.

IV. DISCONTINUOUS-CONDUCTION-MODE SMALL-SIGNAL MODELS

This section details the derivation of the small-signal models of the CL boost converters operating in DCM 1. When the CL converter enters DCM with a duty cycle less than 0.5, the first mode it enters is DCM 1, the waveforms of which are shown in Fig. 6. Once again, the current waveforms of the given mode of operation are used to determine the expressions for v_T and i_{S1} given in equations (4) and (7).
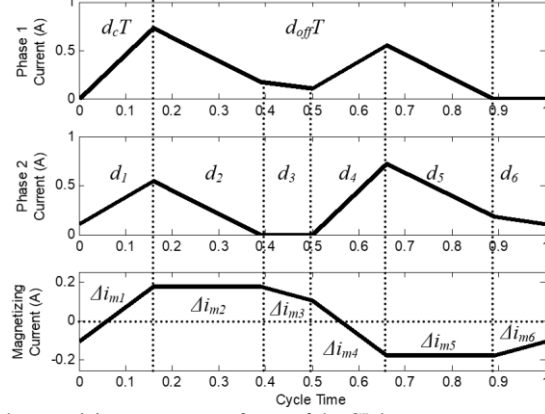

Fig. 6. Phase and magnetizing current waveforms of the CL boost converter operating in DCM 1.

There are six sub-modes of operation of the converter when operating in DCM 1, labeled d_1 to d_6 in Fig. 6 [10]. If balanced operation is assumed, only one phase needs to be analyzed. This analysis focuses on phase 1. As can be seen from Fig. 6, no current flows through phase 1 of the converter during the segment d_6, and so the segment d_6 can be eliminated from the analysis. If d_6 is eliminated, then the total change in magnetizing current, and in turn, the magnetizing inductance voltage, is no longer zero. Hence, to simplify the expression for v_T, it is broken down into its component parts, i.e.

$$(d_c + d_{off})v_T = \sum_{x=1}^{x=5} d_x L_m \frac{di_{mx}}{dt} \tag{26}$$

where x denotes the sub-mode of operation. By analyzing Fig. 6, it is clear that

$$\Delta i_{m1} = -\Delta i_{m4}$$
$$\Delta i_{m2} = \Delta i_{m5} = 0 \tag{27}$$

where Δi_{mx} is the change in the magnetizing current during sub-mode x. Hence, v_T can be simplified to

$$(d_c + d_{off})v_T = L_m \frac{\Delta i_{m3}}{T} \tag{28}$$

The change in magnetizing current during the cycle time d_3 is given by the expression

$$\Delta i_{m3} = \frac{(v_i - v_o)d_3 T}{L_{Lk} + L_m} \tag{29}$$

From Fig. 6, the cycle time d_3 can be expressed as

$$d_3 = 1 - d_c - d_{off} \tag{30}$$

Therefore, the magnetizing element of the inductor voltage equation is expressed as

$$(d_c + d_{off})v_T = L_m \frac{(v_i - v_o)(1 - d_c - d_{off})}{L_{Lk} + L_m} \tag{31}$$

The switch current of DCM 1 occurs during the sub-mode d_1, which is also the cycle time of the peak-to-peak ripple current $\Delta i_{L(p-p)}$. Hence,

$$i_{S1} = \frac{\Delta i_{L(p-p)} d_c}{2} \tag{32}$$

By following the method given in [10], the peak-to-peak inductor current ripple is given by

$$\Delta i_{L(p-p)} = \frac{(2v_i - v_o)d_c T}{2L_{Lk}} + \frac{v_o d_c T}{2(L_{Lk} + 2L_m)} \tag{33}$$

Hence, the switch current of DCM 1 is given by

$$i_{S1} = \left(\frac{(2v_i - v_o)}{L_{Lk}} + \frac{v_o}{(L_{Lk} + 2L_m)} \right) \frac{d_c^2 T}{2} \tag{34}$$

By substituting (31) into (4) and (34) into (7), the dynamic equations are

$$v_{Lk} = L_{Lk} \frac{di_{L1}}{dt} = v_i(d_c + d_{off}) - v_o d_{off} - L_m \frac{(v_i - v_o)(1 - d_c - d_{off})}{L_{Lk} + L_m} - (d_c + d_{off})i_{L1}R_L \tag{35}$$

$$C_{eq} \frac{dv_o}{dt} = 2i_{L1} - 2\left(\left(\frac{(2v_i - v_o)}{L_{Lk}} + \frac{v_o}{(L_{Lk} + 2L_m)} \right) \frac{d_c^2 T}{2} \right) + 2C_o R_C \left(\frac{di_{L1}}{dt} - \frac{d}{dt} \left(\left(\frac{(2v_i - v_o)}{L_{Lk}} + \frac{v_o}{(L_{Lk} + 2L_m)} \right) \frac{d_c^2 T}{2} \right) \right) - \frac{v_o}{R_o} \tag{36}$$

Finally, Table A.1 in the appendix of this paper supplies simultaneous equations which can be used to solve for both d_c and d_{off}. However, since the duty cycle is considered a state, only the expression for d_{off} should be inserted into equations (35) and (36). Once an expression for the diode conduction time is inserted into the above equations; the resulting expressions are linearised, and the unified small-signal models of the CL boost converter operating in DCM 1 are again found as

$$sL_{Lk}\tilde{i}_{L1}(t) = \alpha_1 \tilde{v}_i(s) + \beta_1 \tilde{v}_o(s) + \gamma_1 d_c(s) + \delta_1 \tilde{i}_{L1}(s) \tag{37}$$

$$sC_{eq}\tilde{v}_o(s) = \alpha_2 \tilde{v}_i(s) + \beta_2 \tilde{v}_o(s) + \gamma_2 d_c(s) + \delta_2 \tilde{i}_{L1}(s) \tag{38}$$

Due to the length of the unified coefficients, it is not possible to express them in this paper. In fact, the derivation of the coefficients for all DCM modes of operation is extremely difficult if not found via the use of computational software, such as MATLAB ©. However, by following the method shown in Sections II, III, and IV, and inserting the expressions for v_T and i_{S1} of the desired DCM mode into equations (4) and (7), accurate small-signal models for all modes of operation of the CL boost converter can easily be found. Table A.2 in the appendix presents all expressions for v_T and i_{S1} for all DCM modes of the CL boost converter.

The analysis presented in this section is accurate for balanced operation, i.e. the winding currents and the leakage inductances are equal in both phases. The coupled-inductor used for experimental testing, the CCTT IM, is designed to be strongly coupled, allowing this assumption to be made. However, in all physical systems, imbalances do occur. These imbalances are addressed by controller design, which is discussed for this circuit in [32].

V. UNIFIED TRANSFER FUNCTION MODELS OF THE TWO-PHASE INTERLEAVED BOOST CONVERTER

This section focuses on the derivation of the unified transfer function models of the CL boost converter from the unified small-signal models. Transfer functions are representations of the gain and phase of the linearised system in the frequency domain.

1. Input Voltage-to-Output Voltage Small-Signal Model

The first transfer function to be derived is $G_{vv}(s)$, the input voltage-to-output voltage transfer function. Initially, inductor current in (37) is isolated.

$$\tilde{i}_{L1}(s) = \frac{\alpha_1 \tilde{v}_i(s) + \beta_1 \tilde{v}_o(s) + \gamma_1 d_c(s)}{(sL_{Lk} - \delta_1)} \tag{39}$$

This expression is then substituted into (38).

$$sC_{eq}\tilde{v}_o(s) = \alpha_2 \tilde{v}_i(s) + \beta_2 \tilde{v}_o(s) + \gamma_2 d_c(s) + \delta_2 \frac{\alpha_1 \tilde{v}_i(s) + \beta_1 \tilde{v}_o(s) + \gamma_1 d_c(s)}{(sL_{Lk} - \delta_1)} \tag{40}$$

By gathering all the terms of the dynamic coefficients together, it is found that

$$\tilde{v}_o(s) = \frac{(sL_{Lk}\alpha_2 - \delta_1\alpha_2 + \delta_2\alpha_1)\tilde{v}_i(s) + (sL_{Lk}\gamma_2 - \delta_1\gamma_2 + \delta_2\gamma_1)d_c(s)}{s^2 L_{Lk} C_{eq} - s(L_{Lk}\beta_2 + C_{eq}\delta_1) + (\delta_1\beta_2 - \delta_2\beta_1)} \tag{41}$$

By letting $\tilde{d}_c(s) = 0$, the input voltage-to-output voltage transfer function is found as

$$G_{vv}(s) = \frac{\tilde{v}_o(s)}{\tilde{v}_i(s)} = \frac{(sL_{Lk}\alpha_2 - \delta_1\alpha_2 + \delta_2\alpha_1)}{s^2 L_{Lk} C_{eq} - s(L_{Lk}\beta_2 + C_{eq}\delta_1) + (\delta_1\beta_2 - \delta_2\beta_1)} \tag{42}$$

2. Duty cycle-to-Out Voltage Small-Signal Model

The next transfer function, the duty cycle-to-output voltage transfer function $G_{vd}(s)$, is found by letting $\tilde{v}_i(s)$ equal to zero in (41). Hence,

$$G_{vd}(s) = \frac{\tilde{v}_o(s)}{d_c(s)} = \frac{(sL_{Lk}\gamma_2 - \delta_1\gamma_2 + \delta_2\gamma_1)}{s^2 L_{Lk} C_{eq} - s(L_{Lk}\beta_2 + C_{eq}\delta_1) + (\delta_1\beta_2 - \delta_2\beta_1)} \tag{43}$$

3. Duty Cycle-to-Inductor Current Small-Signal Model

The next transfer function to be derived is the duty cycle-to-inductor current transfer function $G_{id}(s)$. First, the output voltage in (38) is isolated.

$$\tilde{v}_o(s) = \frac{\alpha_2 \tilde{v}_i(s) + \gamma_2 d_c(s) + \delta_2 \tilde{i}_{L1}(s)}{(sC_{eq} - \beta_2)} \tag{44}$$

This expression for the output voltage is then inserted into (37).

$$sL_{Lk}\tilde{i}_{L1}(s) = \alpha_1 \tilde{v}_i(s) + \gamma_1 d_c(s) + \delta_1 \tilde{i}_{L1}(s) + \beta_1 \frac{\alpha_2 \tilde{v}_i(s) + \gamma_2 d_c(s) + \delta_2 \tilde{i}_{L1}(s)}{(sC_{eq} - \beta_2)} \tag{45}$$

By gathering all the terms of the dynamic coefficients together, it is found that

$$\tilde{i}_{L1}(s) = \frac{(sC_{eq}\alpha_1 - \beta_2\alpha_1 + \beta_1\alpha_2)\tilde{v}_i(s) + (sC_{eq}\gamma_1 - \beta_2\gamma_1 + \beta_1\gamma_2)d_c(s)}{s^2 L_{Lk} C_{eq} - s(L_{Lk}\beta_2 + C_{eq}\delta_1) + (\delta_1\beta_2 - \delta_2\beta_1)} \tag{46}$$

Finally, $\tilde{v}_{i(s)}$ is let equal zero, and the duty cycle-to-inductor current transfer function is found to be

$$G_{id}(s) = \frac{\tilde{i}_{L1}(s)}{d_c(s)} = \frac{(sC_{eq}\gamma_1 - \beta_2\gamma_1 + \beta_1\gamma_2)}{s^2 L_{Lk} C_{eq} - s(L_{Lk}\beta_2 + C_{eq}\delta_1) + (\delta_1\beta_2 - \delta_2\beta_1)} \tag{47}$$

4. Inductor Current-to-Output Voltage Small-Signal Model

The final transfer function to be derived is $G_{vi}(s)$, the inductor current-to-output voltage transfer function. In order to find $G_{vi}(s)$, the duty cycle in (38) is isolated.

$$d_c(s) = \frac{sC_{eq}\tilde{v}_o(s) - \alpha_2 \tilde{v}_i(s) - \beta_2 \tilde{v}_o(s) - \delta_2 \tilde{i}_{L1}(s)}{\gamma_2} \tag{48}$$

This expression for the duty cycle is then inserted into (37) and the dynamic coefficients gathered.

$$\tilde{v}_o(s) = \frac{(s\gamma_2 L_{Lk} + \delta_2\gamma_1 - \delta_1\gamma_2)\tilde{i}_{L1}(s) + (\alpha_2\gamma_1 - \alpha_1\gamma_2)\tilde{v}_i(s)}{s\gamma_1 C_{eq} + \beta_1\gamma_2 - \beta_2\gamma_1} \tag{49}$$

Finally, the inductor current-to-output voltage transfer function $G_{vi}(s)$, $\tilde{v}_i(s)$ is set to zero in (49). Hence,

$$G_{vi}(s) = \frac{\tilde{v}_o(s)}{\tilde{i}_{L1}(s)} = \frac{(s\gamma_2 L_{Lk} + \delta_2\gamma_1 - \delta_1\gamma_2)}{(s\gamma_1 C_{eq} + \beta_1\gamma_2 - \beta_2\gamma_1)} \tag{50}$$

The transfer functions represented in (42), (43), (47), and (50) can be applied to the 1L, 2L or CL boost or buck converter.

VI. 1 kW Laboratory Prototype Frequency Sweeps

This section presents experimental frequencies from a two-phase interleaved CL boost converter. These frequency sweeps are used to verify the small-signal models and transfer functions derived in the previous sections. The sweeps are performed on the 1 kW CL boost converter laboratory prototype, shown in Fig. 7. The input of the sweeps is the converter duty cycle, while the output is the output voltage. A dc value of duty cycle containing a small ac sine wave with amplitude of 6% of the dc value to act as the small-signal perturbation is injected into the system. The output voltage is then measured, and the resulting sine wave magnitude and phase is compared to that of the input duty cycle perturbation. This system is presented in Fig. 8. The experimental frequency sweeps begin at 0.01 Hz, and are only accurate up to 1 kHz due to resolution error. The circuit parameters are as follows; leakage inductance L_{Lk} = 350 μH, magnetizing inductance L_m = 1 mH, output capacitance C_o = 900 μF, coupled-inductor ESR R_L = 1 Ω, output capacitor ESR R_C = 170 mΩ, and switching frequency f_s = 16 kHz.. The value of R_L was found using a digital multimeter, while R_C was measured using a PEAK Atlas ESR+ meter [34].
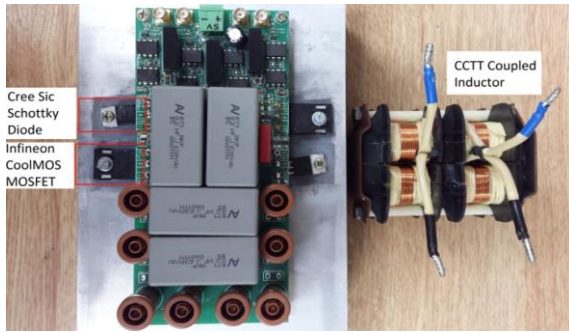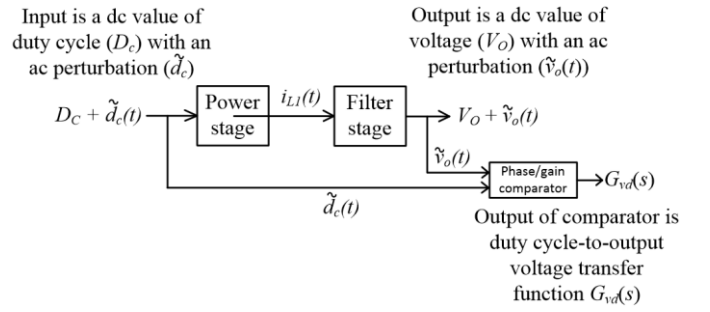

Fig. 7. Prototype CL boost converter.

Fig. 8. Block diagram of experimental frequency sweep from duty cycle to output voltage.

The first frequency sweep is run during CCM operation, the results of which are presented in Fig. 9. As can be seen from Fig. 9, the experimental frequency sweep matches closely to that of the predicted sweep. The inductor current waveform is CCM is presented in Fig. 10. Fig. 11 to Fig. 19 present a comparison between the experimental and theoretical frequency responses of the converter operating in DCM 1, DCM 2, DCM 3, DCM 8, and DCM 9, along with the experimental waveforms of each of the modes [10]. Due to the low current and relatively small operating regions, experimental frequency responses for DCM 4 and DCM 7 are unattainable with this prototype. Table 1 presents the circuit parameters with which each frequency sweep was performed on.
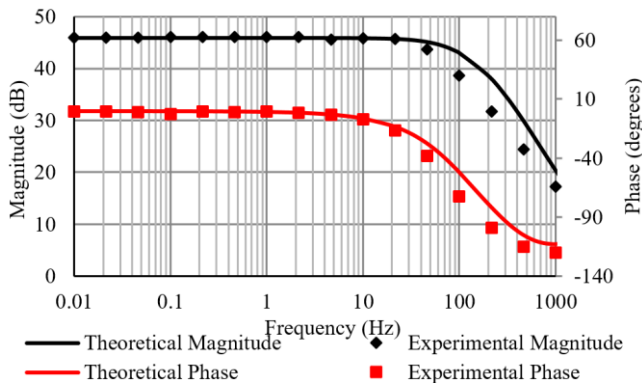

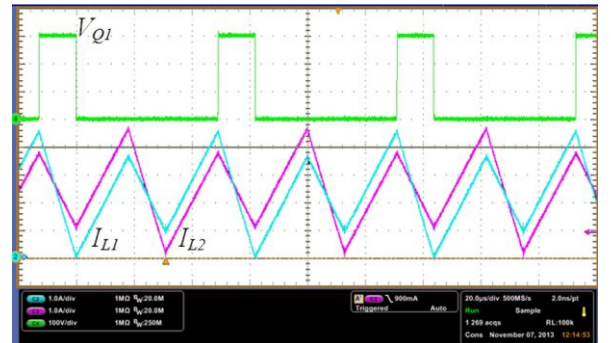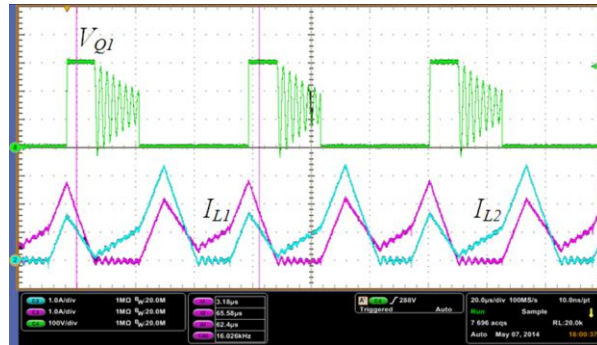Fig. 9. Theoretical and experimental frequency response of the CL converter operating in CCM.
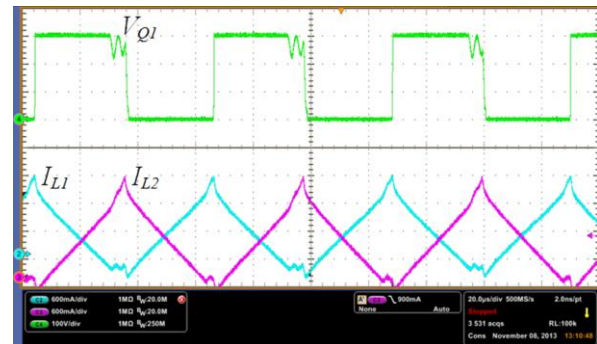

Fig. 10. Experimental waveforms of CCM. The Q1 voltage (green) is 100V/div, while the phase 1 current (blue) and phase 2 current (purple) are 1A/div each [10].

Fig. 11. Theoretical and experimental frequency response of the CL converter operating in DCM 1.

Fig. 12. Experimental waveforms of DCM 1. The Q1 voltage (green) is 100 V/div, while the phase 1 current (blue) and phase 2 current (purple) are 1 A/div each [10].

Fig. 13. Theoretical and experimental frequency response of the CL converter operating in DCM 2.

Fig. 14. Experimental waveforms of DCM 2. The Q1 voltage (green) is 100 V/div, while the phase 1 current (blue) and phase 2 current (purple) are 1 A/div each [10].

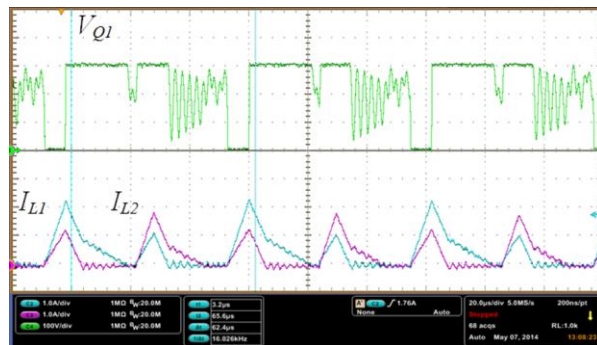Fig. 15. Theoretical and experimental frequency response of the CL converter operating in DCM 3.
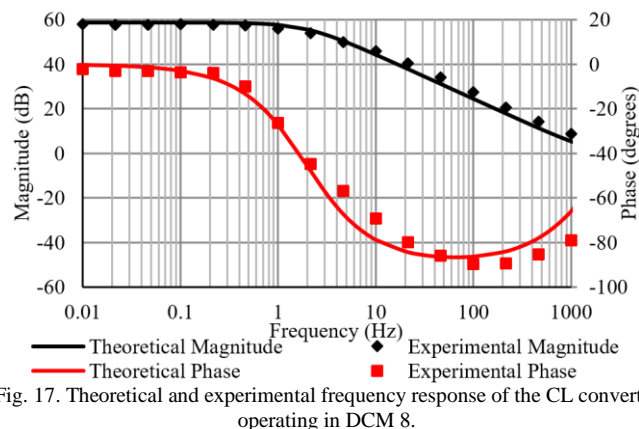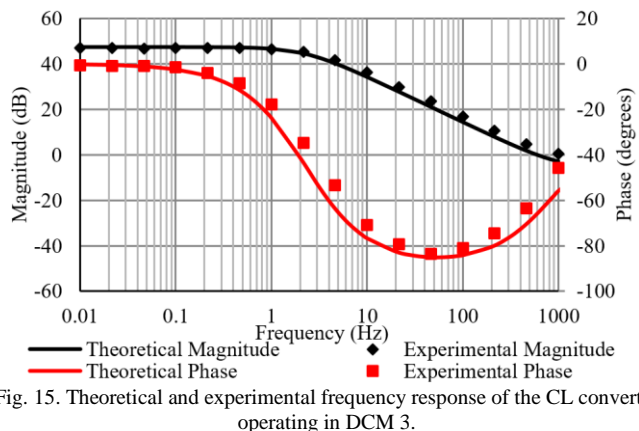

Fig. 16. Experimental waveforms of DCM 3. The Q1 voltage (green) is 100 V/div, while the phase 1 current (blue) and phase 2 current (purple) are 600 mA/div each [10].

Fig. 17. Theoretical and experimental frequency response of the CL converter operating in DCM 8.

Fig. 18. Experimental waveforms of DCM 8. The Q1 voltage (green) is 100 V/div, while the phase 1 current (purple) and phase 2 current (blue) are 1 A/div each [10].

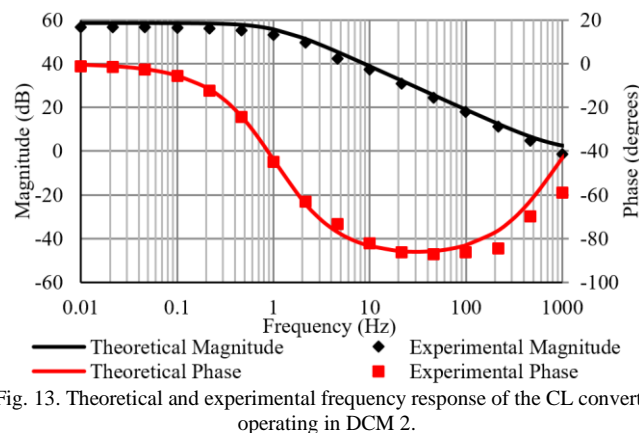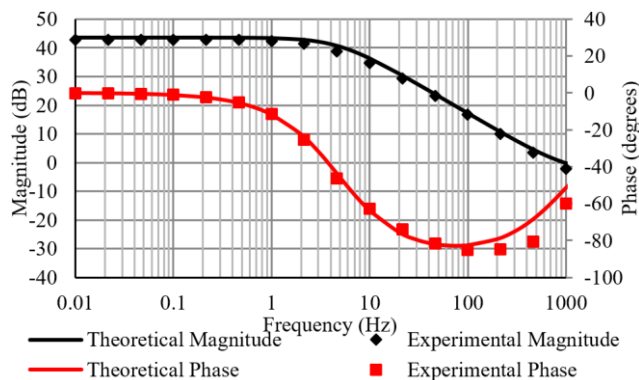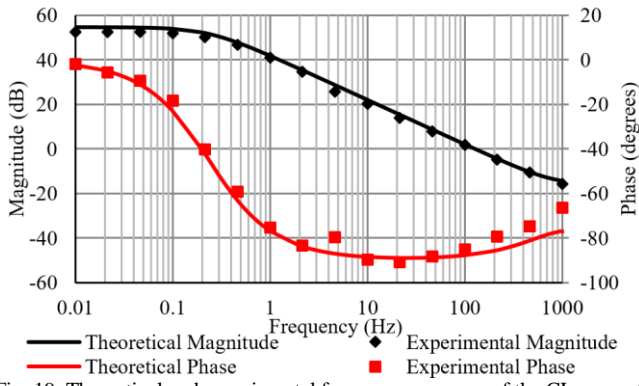Fig. 19. Theoretical and experimental frequency response of the CL converter operating in DCM 9.
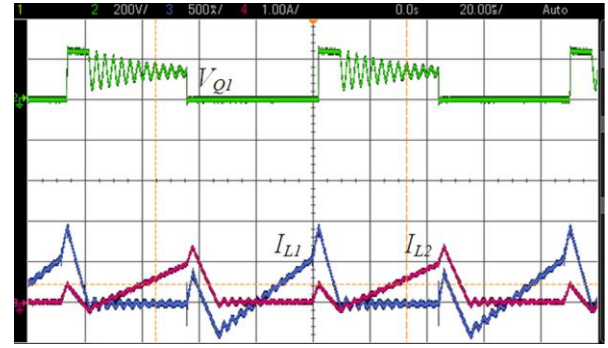

Fig. 20. Experimental waveform of DCM 9. The Q1 voltage (green) is 200 V/div, while the phase 1 current (blue) and phase 2 current (purple) are 500 mA/div and 1 A/div respectively [10].

Table VI.1. Circuit parameters for the various frequency sweep for each mode of operation.

Mode	D_C	V_I	V_O	R_o	I_{L1}
CCM	0.5	50 V	101 V	90 Ω	1.13 A
DCM 1	0.23	70 V	103 V	225 Ω	0.34 A
DCM 2	0.11	200 V	300 V	1020 Ω	0.22 A
DCM 3	0.39	150 V	285 V	507 Ω	0.53 A
DCM 8	0.62	100 V	285 V	330 Ω	0.53 A
DCM 9	0.55	30 V	114 V	2050 Ω	0.1 A

The inclusion of the inductor and capacitor ESRs play a major role in the frequency response when operating in CCM. The calculated frequency response of the converter when the two ESRs are excluded are compared to the calculated response when the ESRs are included, the results of which are presented in Fig. 21 for the inclusion of the inductor ESR only, and Fig. 22 for the inclusion of the capacitor ESR only.
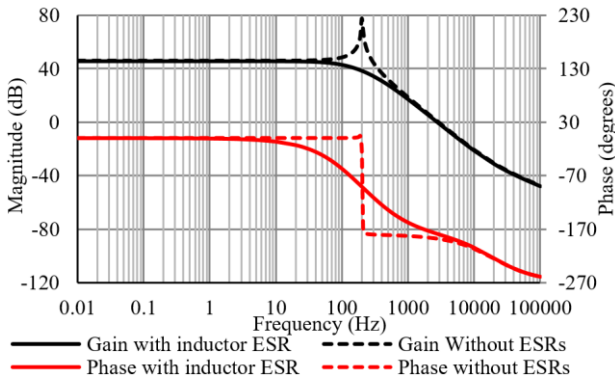

Fig. 21. Theoretical frequency responses of the CL converter operating in CCM with and without inductor ESR.
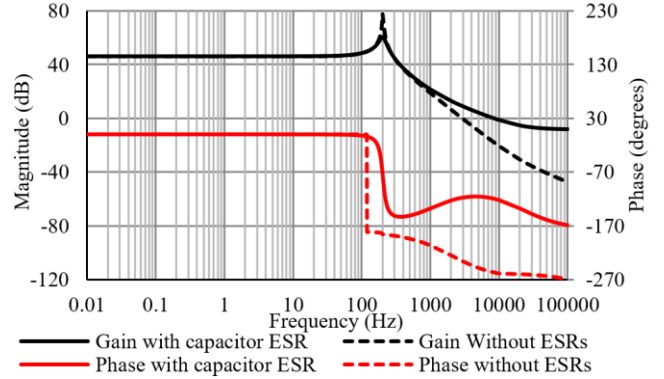

Fig. 22. Theoretical frequency responses of the CL converter operating in CCM with and without capacitor ESR.

As can be seen in Fig. 21 and Fig. 22, a significant resonance occurs at 200 Hz. This resonance is due to the elimination of the coupled-inductor ESR. The phase response of Fig. 21 further shows the effect of the inductor ESR on the resonance. Fig. 22 presents the effects of eliminating the capacitor ESR, which inserts a left-half plane pole which keeps the phase from going below the -180º axis. This effect from the capacitor ESR is visible in all frequency responses of the CL converter. However, when to the converter operates in DCM, the inductor ESR does not have such a significant effect on the response. As can be seen from the resulting frequency response, the predicted responses match quite closely with the measured responses. The effect of the capacitor ESR at higher frequencies is also evident, as it causes a rise in the phase in each frequency response. A theoretical plot comparing the frequency sweeps of DCM 1 operating with, and without, capacitor ESR is presented in Fig. 23, while Fig. 24 presents the frequency sweeps with and without the inductor ESR. These plots are developed by using the transfer function presented in equation (43).
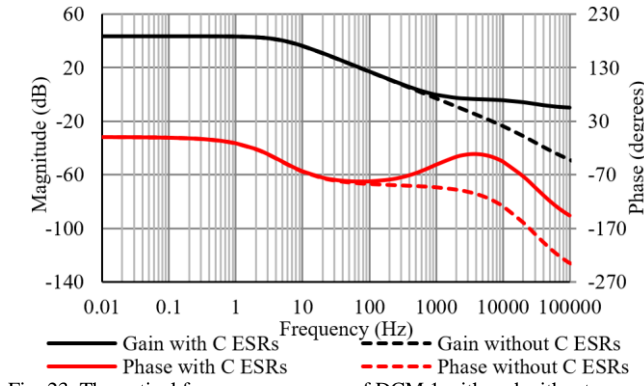
Fig. 23. Theoretical frequency response of DCM 1 with and without capacitor ESR.
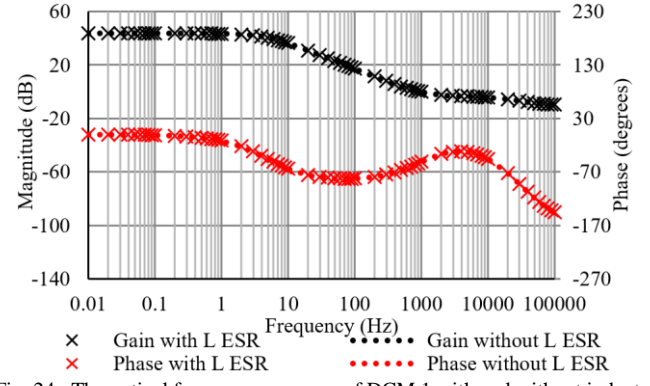

Fig. 24. Theoretical frequency response of DCM 1 with and without inductor ESR.

As can be seen from Fig. 23, the output capacitor ESR plays a major role in the gain and phase at higher frequencies. If a controller is to be designed at such high frequencies, then the capacitor ESR must be included in the small-signal model. However, as can be seen from Fig. 24, the inductor ESR has very little on the frequency sweep. This is in contrast to CCM operation, where the inductor ESR significantly dampens the resonance of the converter. These sweeps not only validate the dynamic equations utilized to find the small-signal models, but also the method.

Finally, the theoretical frequency sweep DCM 1 is compared to a simulated frequency sweep performed in Matlab SimPowerSystems in order to validate the models at higher frequencies. This comparison is presented in Fig. 25.
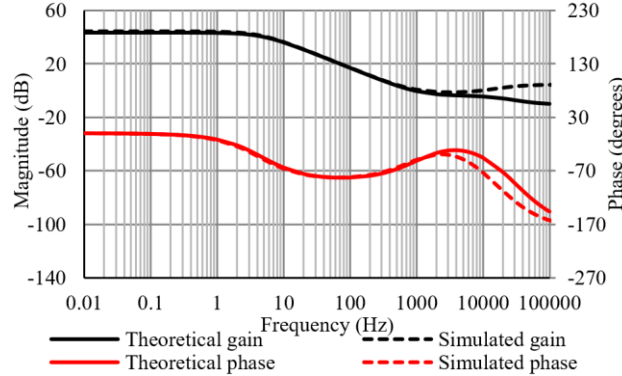

Fig. 25. Theoretical and simulated frequency response of DCM 1.

As can be seen, the theoretical plots match closely to the simulated plots. However, note must be taken as to the upper frequency limit of the small-signal model. Due to the fact that a boost converter is heavily reliant on the switching frequency, the rapid change of duty cycle any higher than half the switching frequency may lead to inconsistencies between the theoretical sweeps and the physical converter sweeps. This is also evident in Fig. 25, in which a simulated converter with a switching frequency of 16 kHz begins to deviate at frequency close to half the switching frequency i.e. 8 kHz.

VII. CONCLUSIONS

The dynamic operation of a coupled-inductor boost converter operating in DCM is the novel subject of this investigation. Implementing a coupled-inductor into an interleaved boost converter introduces several DCM modes of operation, which have not been analyzed in the small-signal domain. This paper derives the small-signal model and transfer functions of a coupled-inductor boost converter. Initially, the dynamic equations required to begin deriving the small-signal models are developed. Example derivations of the small-signal models of CCM and one DCM mode are presented. These derivations can then be extended to all other modes of operation. The unified transfer functions are then derived. Finally, the small-signal models and transfer functions are then validated by experimental frequency sweeps of a 1 kW laboratory prototype.

VIII. REFERENCES

[1] L. Palma and P.N. Enjeti, "Modular fuel cell, modular DC–DC converter concept for high performance and enhanced reliability," *IEEE Transactions on Power Electronics,* vol. 24, no. 6, pp. 1437-1443, June 2009.

[2] K. Jin, X. Ruan, M. Yang, and M. Xu, "Hybrid fuel cell power system," *IEEE Transactions on Industrial Electronics,* vol. 56, no. 4, pp. 1212-1222, April 2009.

[3] S. Chandrasekaran and L. U. Gokdere, "Integrated magnetics for interleaved dc-dc boost converter for fuel cell powered vehicles," *IEEE Power Electronics Specialists Conference,* vol. 1, pp. 356-361, June 2004.

[4] B.J. Masserant, E.W. Beans, T.A. Stuart, "A study of volume versus frequency for soft switching IGBT converters," *IEEE Transactions on Aerospace and Electronic Systems*, Vol. 31, No. 1, January 1995, pp. 280-287.

[5] D.Y. Jung, Y.H. Ji, S.H. Park, Y.C. Jung, and C.Y. Won, "Interleaved soft-switching boost converter for photovoltaic power-generation system," *IEEE Transactions on Power Electronics*, vol. 26, no. 4, pp. 1137-1145, Apr. 2011.

[6] S. Chandrasekaran and L.U. Gokdere, "Integrated magnetics for interleaved dc-dc boost converter for fuel cell powered vehicles," 35th Annual *IEEE Power Electronics Specialists Conference*, pp. 356-361, June 2004.

[7] Y.P. Siwakoti and F. Blaabjerg, "Single Switch Nonisolated Ultra-Step-Up DC–DC Converter With an Integrated Coupled Inductor for High Boost Applications," in *IEEE Transactions on Power Electronics*, vol. 32, no. 11, pp. 8544-8558, Nov. 2017..

[8] G. Calderon-Lopez and A.J. Forsyth, "Sampled-data analysis of the dual-interleaved boost converter with interphase transformer," *IEEE Transactions on Power Electronics,* vol. 27, no. 3, pp. 1338-1346, August 2011.

[9] G. Calderon-Lopez and A.J. Forsyth, "High-power dual-interleaved ZVS boost converter with interphase transformer for electric vehicles," *24th Annual Applied Power Electronics Conference and Exposition*, pp. 1078-1083, February 2009.

[10] B.C. Barry, J.G. Hayes, and M.S. Ryłko, "CCM and DCM operation of the interleaved two-phase boost converter with discrete and coupled inductors," *IEEE Transaction on Power Electronics*, vol. 30, no. 12, pp. 6551-6567, December 2015.

[11] K. J. Hartnett, J.G. Hayes, M. Ryłko, B. C. Barry, and J. W. Masłoń, "Comparison of 8-kW CCTT IM and discrete inductor interleaved boost converter for renewable energy applications," *IEEE Transaction on Industry Applications*, vol. 51, no. 3, pp. 2455-2469, May 2015.

[12] K.J. Hartnett, J.G. Hayes, M.G. Egan, and M.S. Ryłko, "CCTT-core split-winding integrated magnetic for high-power DC-DC converters," *IEEE Transactions on Power Electronics*, vol. 28, no. 11, pp. 4970-4974, November 2013.

[13] N. Kondrath, and M.K. Kazimierczuk, "Control-to-output transfer function of peak current mode controlled pulse-width modulated dc–dc buck converter in continuous conduction mode", *IET Power Electronics*, vol. 5, no. 5, pp. 582-590, May 2012.

[14] J. D. Dasika, B. Bahrani, M. Saeedifard, A. Karimi and A. Rufer, "Multivariable Control of Single-Inductor Dual-Output Buck Converters", *IEEE Transactions on Power Electronics*, vol. 29, no. 4, pp. 2061-2070, June 2013.

[15] A. Reatti and M.K. Kazimierczuk, "Small-signal model of PWM converters for discontinuous conduction mode and its application for boost converter", *IEEE Transactions on Circuits and Systems I: Fundamental Theory and Applications*, vol. 50, no. 1, pp. 65-73, January 2003.

[16] B. Bryant and M.K. Kazimierczuk, "Voltage loop of boost PWM DC-DC converters with peak current-mode control", *IEEE Transactions on Circuits and Systems I: Regular Papers*, vol. 53, no. 1, pp. 99-105, January 2006.

[17] Q. Wang, L. Shi and C. Chang, "Small-signal transfer functions for a single-switch buck-boost converter in continuous conduction mode", *9th International Conference on Solid-State and Integrated-Circuit Technology*, Beijing, pp. 2016-2019, 2008.

[18] M.C. Lee, J.B. Lio, D.Y. Chen, Y.T. Chen and Y.P. Wu, "Small-signal modeling of multiple-output flyback converters in continuous conduction mode with weighted feedback" *IEEE Transactions on Industrial Electronics*", vol. 45, no. 2, pp. 236-248, April 1998.

[19] A.C. Schittler, D. Pappis, A. Campos, M.A. Dalla Costa and J.M. Alonso, "Interleaved Buck Converter Applied to High-Power HID Lamps Supply: Design, Modeling and Control," *IEEE Transactions on Industry Applications*, vol. 49, no. 4, pp. 1844-1853, July-Aug. 2013.

[20] L. Ni, D.J. Patterson and J.L. Hudgins, "High Power Current Sensorless Bidirectional 16-Phase Interleaved DC-DC Converter for Hybrid Vehicle Application," in *IEEE Transactions on Power Electronics*, vol. 27, no. 3, pp. 1141-1151, March 2012.

[21] A. Marcos-Pastor, E. Vidal-Idiarte, A. Cid-Pastor and L. Martinez-Salamero, "Interleaved Digital Power Factor Correction Based on the Sliding-Mode Approach," in *IEEE Transactions on Power Electronics*, vol. 31, no. 6, pp. 4641-4653, June 2016.

[22] M. Veerachary, T. Senjyu and K. Uezato, "Modeling and analysis of interleaved dual boost converter," *ISIE 2001. 2001 IEEE International Symposium on Industrial Electronics Proceedings (Cat. No.01TH8570)*, pp. 718-722 vol.2 Pusan, 2001.

[23] H.B. Shin, E.S. Jang, J.G. Park, H.W. Lee and T.A. Lipo, "Small-signal analysis of multiphase interleaved boost converter with coupled inductors," in *IEE Proceedings - Electric Power Applications*, vol. 152, no. 5, pp. 1161-1170, 9 Sept. 2005.

[24] Y.S. Lee, "A systematic and unified approach to modeling switches in switch-mode power supplies," *IEEE Transactions on Industrial Electronics*, vol. IE-32, pp. 445–448, Nov. 1985.

[25] V. Vorperian, "Simplified analysis of PWM converters using the PWM switch, Part I: Continuous conduction mode," *IEEE Transactions on Aerospace and Electronic Systems*, vol. 26, pp. 497–505, May 1990.

[26] V. Vorperian, "Simplified analysis of PWM converters using the PWM switch, Part II: Discontinuous conduction mode," *IEEE Transactions on Aerospace and Electronic Systems*, vol. 26, pp. 497–505, May 1990.

[27] A. Pietkiewicz and D. Tollik, "Unified topological modeling method of switching dc–dc converters in duty-ratio programmed mode," *IEEE Transactions on Power Electronics*, vol. PE-2, no. 3, pp. 218–226, 1987.

[28] T.F. Wu, and Y.K. Chen, "Modeling PWM DC/DC Converters Out of Basic Converter Units", *IEEE Transactions on Power Electronics*", vol. 13, no. 5, pp. 870-881, September 1998.

[29] M. Veerachary, "Signal flow graph modelling of multi-state boost DC-DC converters," in *IEE Proceedings - Electric Power Applications*, vol. 151, no. 5, pp. 583-589, 9 Sept. 2004.

[30] M. Veerachary, "Modeling of Power Electronic Systems Using Signal Flow Graphs," *IECON 2006 - 32nd Annual Conference on IEEE Industrial Electronics*, Paris, 2006, pp. 5307-5312.

[31] B.C. Barry, J.G. Hayes, M.S. Rylko, R. Stala, A. Penczek, A. Mondzik, R.T. Ryan, "Small-signal model and control of the interleaved two-phase coupled-inductor boost converter," 2016 *IEEE Energy Conversion Congress and Exposition* (ECCE), Milwaukee, WI, 2016, pp. 1-6.

[32] B.C. Barry, J.G. Hayes, M.S. Rylko, R. Stala, A. Penczek, A. Mondzik, R.T. Ryan, " Digital type II compensation with forced-output control of an interleaved two-phase coupled-inductor boost converter," *2017 IEEE Energy Conversion Congress and Exposition* (ECCE), Cincinnati, OH, 2016, pp. 1-6.

[33] R.W. Erickson, (1997), *Fundamentals of Power Electronics*, Kluwer Academic Publishers.

[34] N. Mohan, T.M. Underland, and W.P. Robbins, (1995), *Power Electronics, Converters, Applications, and Designs*, Wiley.

[35] http://www.peakelec.co.uk/acatalog/jz_esr70.html [Last accessed 26/08/2017].

IX. APPENDIX

Table A.1. Simultaneous Equations required for solving d_c and d_{off} for each DCM mode of operation.

Mode	Find	
	d_c	$(d_c + d_{off})v_i - d_{off}v_o - v_T = 0$
	d_{off}	$i_{L1} - \dfrac{T}{4}\left(\dfrac{(v_o - v_i)(1 - 2d_{off}) + 2(2v_i - v_o)(d_c^2 + d_c d_{off})}{L_{Lk}} - \dfrac{v_o d_c}{L_{Lk} + 2L_m} - \dfrac{(2d_c + 1)(v_o - v_i)(d_c + d_{off} - 1)}{L_{Lk} + L_m} \right) = 0$
	d_c	$(d_c + d_{off})v_i - d_{off}v_o - v_T = 0$
	d_{off}	$i_{L1} + \dfrac{T}{8}\left(\dfrac{v_o d_c(d_c - d_3 - 3d_{off})}{L_{Lk} + 2L_m} + \dfrac{v_o d_c(d_3 - d_{off}) - (4v_i - 3v_o)d_c^2 - 4(v_o - v_i)\left(\dfrac{d_c}{2} + \dfrac{d_3}{2} - \dfrac{d_{off}}{2}\right)^2}{L_{Lk}} \right)$ where $d_3 = \dfrac{v_o d_c(L_{Lk} + L_m)}{(L_{Lk} + 2L_m)(v_o - v_i)}$
	d_c	$(d_c + d_{off})v_i - d_{off}v_o - v_T = 0$
	d_{off}	$i_{L1} + \dfrac{T\left(v_i(d_c + d_{off} - 1) + v_o d_{off}(1 - 2d_c)\right)}{4(L_{Lk} + L_m)} - \left(\dfrac{v_o}{L_{Lk} + 2L_m} - \dfrac{(v_o - 2v_i)}{L_{Lk}}\right)\dfrac{(2d_c + 2d_{off} - 1)T}{8} = 0$
	d_c	$(d_c + d_{off})v_i - d_{off}v_o - v_T = 0$
	d_{off}	$i_{L1} - \dfrac{v_i d_c T(d_c + d_{off})}{L_{Lk} + L_m}$
	d_c	$(d_c + d_{off})v_i - d_{off}v_o - v_T = 0$
	d_{off}	$i_{L1} + \dfrac{T}{4}\left(\dfrac{2v_i(d_c - d_{off}) - 4v_i(d_c^2 - d_{off}^2) + v_o(d_{off} - 2d_{off}^2)}{L_{Lk}} - \dfrac{v_o d_{off}}{L_{Lk} + 2L_m} - \dfrac{2v_i(d_c - d_c^2 + d_{off}^2 - d_{off})}{L_{Lk} + L_m} \right) = 0$
	d_c	$(d_c + d_{off})v_i - d_{off}v_o - v_T = 0$
	d_{off}	$i_{L1} + \dfrac{T}{4}\left(\dfrac{2v_i(d_c - d_{off}) - 4v_i(d_c^2 - d_{off}^2) + v_o(d_{off} - 2d_{off}^2)}{L_{Lk}} - \dfrac{v_o d_{off}}{L_{Lk} + 2L_m} - \dfrac{2v_i(d_c - d_c^2 + d_{off}^2 - d_{off})}{L_{Lk} + L_m} \right) = 0$
	d_c	$(d_c + d_{off})v_i - d_{off}v_o - v_T = 0$
	d_{off}	$i_{L1} + \dfrac{T}{4}\left(\dfrac{2v_i(d_c - d_{off} - 2d_c^2 + 2d_{off}^2) + v_o(d_{off} - 2d_{off}^2)}{L_{Lk}} - \dfrac{v_o d_{off}}{L_{Lk} + 2L_m} - \dfrac{2v_i(d_c - d_c^2 + d_{off}^2 - d_{off})}{L_{Lk} + L_m} \right) = 0$

Table A.2. Magnetizing inductance voltage and switch current of each DCM mode of operation

Mode	
	$$v_T = L_m \frac{(1 - d_c - d_{off})(v_i - v_o)}{L_{Lk} + L_m}$$
	$$i_{S1} = \frac{d_c^2 T}{4}\left(\frac{v_o}{L_{Lk} + 2L_m} - \frac{v_o - 2v_i}{L_{Lk}} \right)$$
	$$v_T = L_m \frac{-v_o d_c}{L_{Lk} + 2L_m}$$
	$$i_{S1} = \frac{d_c^2 T}{4}\left(\frac{v_o}{L_{Lk} + 2L_m} - \frac{v_o - 2v_i}{L_{Lk}} \right)$$
	$$v_T = L_m \frac{v_i(0.5 - d_{off}) + (v_o - v_i)(0.5 - d_c)}{L_{Lk} + L_m}$$
	$$i_{S1} = \frac{T}{8}\left(\frac{v_i(2d_{off} - 1)^2}{L_{Lk} + L_m} + \frac{v_o(4d_c^2 - 4d_{off}^2 + 4d_{off} - 1)}{2(L_{Lk} + 2L_m)} - \frac{(v_o - 2v_i)(4d_c^2 - 4d_{off}^2 + 4d_{off} - 1)}{2L_{Lk}} \right)$$
	$$v_T = 0$$
	$$i_{S1} = \frac{v_i d_c^2 T}{L_{Lk} + L_m}$$
	$$v_T = L_m \frac{v_i(1 - d_c - d_{off})}{L_{Lk} + L_m}$$
	$$i_{S1} = \frac{T}{4}\left(\frac{v_o(d_{off} - d_{off}^2)}{L_{Lk} + 2L_m} + \frac{2v_i(d_c - d_c^2 + d_{off}^2 - d_{off})}{L_{Lk} + L_m} - \frac{2v_i(d_c - d_{off} - 2d_c^2 + d_{off}^2) + v_o(d_{off} - d_{off}^2)}{L_{Lk}} \right)$$
	$$v_T = L_m \frac{v_i(1 - d_c - d_{off})}{L_{Lk} + L_m}$$
	$$i_{S1} = \frac{T}{4}\left(\frac{v_o(d_{off} - d_{off}^2)}{L_{Lk} + 2L_m} + \frac{2v_i(d_c - d_c^2 + d_{off}^2 - d_{off})}{L_{Lk} + L_m} - \frac{2v_i(d_c - d_{off} - 2d_c^2 + d_{off}^2) + v_o(d_{off} - d_{off}^2)}{L_{Lk}} \right)$$
	$$v_T = L_m \frac{v_i(1 - d_c - d_{off})}{L_{Lk} + L_m}$$
	$$i_{S1} = \frac{T}{4}\left(\frac{2v_i(d_c - d_c^2 + d_{off}^2 - d_{off})}{L_{Lk} + L_m} - \frac{2v_i(d_c - d_{off} + d_{off}^2 - 2d_c^2) - v_o(d_{off}^2 - d_{off})}{L_{Lk}} - \frac{v_o(d_{off}^2 - d_{off})}{L_{Lk} + 2L_m} \right)$$